Influence of CO_2-Ar Mixtures as Shielding Gas on Laser Welding of Al-Mg Alloys

ZOUHAIR BOUKHA, JOSÉ MARÍA SÁNCHEZ-AMAYA, LEANDRO GONZÁLEZ-ROVIRA, ELOY DEL RIO, GINESA BLANCO, and JAVIER BOTANA

In this study, AA5083 samples were butt welded under a conduction regime with high-power diode laser (HPDL). Various mixtures composed of Ar and CO_2 were used as a shielding gas. The influence of the shielding gas composition on the microstructure and on the properties of laser welds was analyzed. The weld beads were deeply characterized by metallographic/microstructural studies, X-ray diffraction (XRD), X-ray energy dispersive spectrometry (X-EDS) chemical analyses, X-ray photoelectron spectra (XPS), microhardness, and tensile strength. The corrosion resistance of laser-remelted surfaces with different CO_2/Ar ratios was also estimated by means of electrochemical tests. The addition of CO_2 to the shielding gas results in a better weld penetration and oxidizes the weld pool surface. This addition also promotes the migration of Mg toward the surface of weld beads and induces the formation of magnesium aluminates spinel on the welds. The best corrosion resistance result is achieved with 20 pct CO_2. The overall results indicate that the addition of small percentage of CO_2 to Ar leads to improvements of the mechanical and corrosion properties of the aluminum welds.

DOI: 10.1007/s11661-013-1953-y

I. INTRODUCTION

TRADITIONAL welding processes present a series of disadvantages when applied to aluminum alloys, which have sometimes discouraged the use of such welded materials. The poor welding reliability of aluminum alloys lies in their physical properties, especially their high thermal conductivity, high reflectivity, and low viscosity.[1] During the last two decades, significant and improved solutions for welding aluminum alloys have been developed.[2–5] Laser welding is now a competitive alternative to the conventional technologies (GMAW and GTAW), presenting important advantages such as the low heat input, high localization ability, high welding speed, high flexibility, high weld quality, and high production rate.[6–11] Numerous studies dealing with laser welding of aluminum alloys are available.[6–13] Although the majority of them are performed under keyhole regime, recent research projects are alternatively using conduction regime because it has the advantage of reducing the formation of porosity, cracks, and undercutting in the welds. In addition to these well-known regimes, AssunÇao *et al.*[14] have just proved the existence of a third welding mode so-called transition regime, leading to welds with characteristics of both keyhole (undercut, not flat top profile, and small depression at the surface) and conduction (low aspect ratio).

High-power CO_2[8–11] and neodymium-doped yttrium aluminium garnet (Nd:YAG)[6,7,15] lasers are the most common equipments employed to weld aluminum alloys. High-power diode laser (HPDL) has been used in fewer works,[16–21] although it offers a clear advantage: The absorption of the HPDL wavelength by aluminum alloys is higher than the CO_2 and Nd:YAG wavelengths.[19] Thus, the emission wavelength of the HPDL (808 nm) provokes a higher absorptivity in aluminum than the longer wavelengths of Nd:YAG (1064 nm) and CO_2 (10640 nm) lasers. As a consequence, HPDL is being widely used in surface engineering technology.[22,23]

To preserve the properties of materials during laser welding, shielding gas is of crucial importance to prevent embrittlement of the weld region and avoid losses in ductility.[24–28] Protection of the weld pool against atmospheric contaminations is performed by means of shielding gas, which has also been reported to improve the laser-material coupling.[24] In addition to protecting the molten material from oxidation, shielding gas can, however, induce welding defects such as porosity and cracks. The main reason of the porosity formation in welding processes is the gas bubbles entrapment in the

ZOUHAIR BOUKHA, Researcher, and JAVIER BOTANA, Professor, are with the LABCYP, Departamento de Ciencia de los Materiales e Ingeniería Metalúrgica y Química Inorgánica, CASEM, Universidad de Cádiz, Campus Río San Pedro, 11510 Puerto Real, Cádiz, Spain. JOSÉ MARÍA SÁNCHEZ-AMAYA, and LEANDRO GONZÁLEZ-ROVIRA, Researchers, are with the LABCYP, Departamento de Ciencia de los Materiales e Ingeniería Metalúrgica y Química Inorgánica, CASEM, Universidad de Cádiz, and also with the Titania, Ensayos y Proyectos Industriales S.L. Parque Tecnológico TecnoBahía Edif. RETSE, Nave 4. Ctra. Sanlúcar Km 7, 11510 El Puerto de Santa María, Cádiz, Spain. Contact e-mail: josemaria.sanchez@uca.es ELOY DEL RIO, Researcher, and GINESA BLANCO, Professor, are with the IMEYMAT, Departamento de Ciencia de los Materiales e Ingeniería Metalúrgica y Química Inorgánica, Facultad de Ciencias, Universidad de Cádiz.

Manuscript submitted February 14, 2013.
Article published online September 17, 2013

molten material, which cannot escape before solidification.[25]

The influence of the shielding gas composition (Ar, He, N_2, CO_2, or their mixtures) on weld penetration has been analyzed in the recent literature.[15,29–31] Concerning the nature of the shielding gas, contradictory results can be found.[24,32] Thus, low-density gases are reported in Reference 32 to diffuse more easily in the welds, providing worse protection than denser gases. However, Wang *et al.*[24] claimed that He has a higher protection effect than Ar. High-density gases (Ar) can be kept for longer times at the welding zone but also have a higher absorption coefficient (leading to the absorption of higher laser radiation) than low-density gases (He). These two effects can vary depending on the laser type and alloys, explaining the divergence of the results. N_2 has also been applied to shield the laser welding of aluminum alloys, leading to good quality (free of porosity) weld beads.[21,30] Adding to Ar a small amount of gas containing minor elements is a way to accomplish the transfer of the minor elements to the weld pool by adjusting the chemical composition to the base material and increase the weld penetration.[26–28,33–35] The effect of Ar/He gas ratio on melting different aluminum alloys (5052, 5083, 5182, 6061, and 7N01) has been investigated, revealing that the use of Ar is beneficial when welding more highly conductive and reflective alloys at lower power and higher welding speed, while a higher content of He is preferred for higher power and lower welding speed.[31] Likewise, mixtures of Ar-CO_2 or He-Ar-O_2[32] have been demonstrated to improve the penetration of hybrid LASER–MIG welds of stainless steel.

In large quantities, semi-inert shielding gases (also known as active shield gases) including carbon dioxide, oxygen, nitrogen, and hydrogen, would damage the weld, but when used in small, controlled quantities, can improve weld characteristics.[36] The benefits of using carbon dioxide as shielding gas for laser welding are that it is cheaper than helium and argon and that it provides nearly the same penetration as helium. Also, the addition of carbon dioxide to argon provides a significant source of oxygen absorption for the molten weld metal (WM). The controlled presence of oxygen in the weld pool has been reported to have positive effects on the penetration and the shape of the steel welds.[37] However, the concise influence of CO_2 additions on the shielding gas in laser welding of aluminum alloys has not been explored yet in the literature.

In our previous studies, HPDL has been successfully employed to weld different aluminum alloys employing Ar or N_2 as shielding gas.[16,17,20,21,38–40] In the current work, progressive additions of CO_2 to Ar have been used as shielding gases in the laser welding of 5083 aluminum alloy. The obtained results operating in pure Ar, pure CO_2, and different CO_2-Ar mixtures are presented. Furthermore, the effect of the CO_2/Ar ratio on the morphology, microstructure, surface distributions of Al and Mg, crystalline phases evolution, mechanical properties, and corrosion resistance of 5083 butt welds are reported.

II. EXPERIMENTAL

Commercial AA5083 sheets of 3 mm thickness were used as base material. This specific alloy is chosen for being a reference material in laser welding studies of our research group; its laser weldability is known and proved in our previous investigations.[16,17,20,21,38,39] These AA5083 sheets were cut to obtain the required samples size for each test. Before laser treatments, the work pieces were first sandblasted with white corindon particles and subsequently chemically cleaned with acetone to eliminate surface contamination. This superficial treatment was seen to improve laser absorption in comparison with the grinding process.[16]

All laser treatments were performed with a HPDL (Rofin-Sinar DL028S; ROFIN-SINAR Laser GmbH, Hamburg, Germany). Figure 1 includes schemes of the three different laser treatments applied to 5083 samples: butt welding in schemes A and C and laser remelting in scheme B, being the scheme B only employed to characterize the corrosion behavior. The butt welds were performed by a linear laser scan of 60 mm at the interface of the two samples (schemes A and C of Figure 1), while laser-remelting treatments consisted of 11 parallel scans of 60 mm with a 25 pct of overlapping (scheme B of Figure 1). Most laser welding treatments were performed to pairs of samples of 70 mm long and 14 mm wide (scheme A of Figure 1), the HPDL working in continuous mode at 2.5 kW and at laser processing rate of 1 m/min. Only the samples devoted to tensile tests were 70 mm long and 50 mm wide (scheme C of Figure 1), allowing one to obtain welded samples of 70 mm × 100 mm. These latter samples were butt welded on both sides at 2.5 kW and 0.3 m/min to obtain full penetration welds.

The CO_2/Ar ratio in the shielding gas was changed from 0 pct up to 100 pct of CO_2, working at a flow rate of 15 L/min. The parameters of the laser beam employed to generate butt welds and remelting treatments under conduction regime are included in Table I. All treatments and measurements have been performed in triplicate to assure the results reproducibility.

Cross-sections of all weld beads were prepared and subsequently etched with a Keller solution to reveal the microstructure, shape, and bead dimensions, which were analyzed by optical microscopy. Vickers microhardness

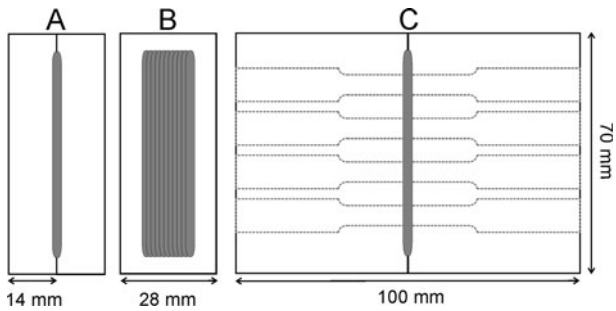

Fig. 1—Schematical representation of butt welding and laser-remelting treatments.

measurements were also carried out on transversal sections of weld beads according to the standard ASTM E-384.[41] The charge employed was 490.3 mN during 19 seconds. Microhardness maps and profiles of representative welds have been measured, following the scheme of Figure 2.

Transmission electron microscopy (TEM) observations were carried out with a JEOL 1200X microscope (JEOL Ltd., Tokyo, Japan) equipped with thermionic electron source and operating at 120 kV. Sections of the samples were obtained in an ultramicrotome EM UC6 from Leica Microsystems (Buffalo Grove, IL) employing a diamond knife.

X-ray energy dispersive spectrometry (X-EDS) chemical analyses were performed using a Phoenix-EDAX equipment coupled at a Quanta 200-FEI microscope (FEI Company, Hillsboro, OR). This technique was principally employed to evaluate the variation of magnesium amount between the base metal (BM) and fusion zone of the welds.

The ultimate tensile stress of generated butt welds was determined by tensile tests. Three specimens were taken from each welded plate, and the final shape and size of the test specimens are shown in Figure 3. The tests were accomplished at room temperature in a Shimadzu test machine (Shimadzu Corporation, Kyoto, Japan) with a capacity of 100-kN load at the initial strain rate of 6 $N \cdot mm^{-2} \cdot s^{-1}$. The influence of CO_2 additions of shielding gas on the tensile strength measurements was determined.

X-ray diffraction (XRD) studies were carried out on a Bruker instrument (model D8 Advance, radius 250 mm; Bruker AXS, Billerica, MA). The diffractograms were recorded under the following conditions: Cu Kα radiation, with graphite monochromator, scan range from 3 deg up to 75 deg, with a step size of 0.07 deg and a time per step of 40 seconds. Crystalline phases were identified by comparison with literature data.

The X-ray photoelectron spectra (XPS) were recorded on Kratos Axis Ultra DLD spectrometer (Kratos Surface Analysis, Manchester, U.K.). The selected X-ray source was monochromatized Al Kα radiation (1486.6 eV) operating at 150 W. Electrostatic charging effects could be stabilized with the help of a charge neutralizer system developed by Kratos. The transfer of the samples to the analysis chamber was carried out under ultrahigh vacuum conditions (~10^{-9} Torr). A 160-eV pass energy was selected to record the low-resolution wide-range spectra. For the high-resolution spectra, a pass energy of 20 eV was used, corresponding to an energy resolution of 1.1 eV for the full width at half-maximum (FWHM) of the Au $4f_{7/2}$ component. The collected data came from Al 2p, O 1s, and C 1s core levels. The binding energy (BE) scale was calibrated with respect to the C 1s signal (284.8 eV) for adventitious carbon and given with an accuracy of 0.1 eV. Spectra processing was performed using CasaXPS software (version 2.3.15; Casa Software Ltd, Devon, U.K.). In all cases, a Shirley-type background was applied. Peak decomposition of Al 2p core level was performed by using Doniach-Sunjic line shapes for metallic Al and mixed Gaussian/Lorentzian shape for aluminum oxide component of the spectra. Aluminum oxide thicknesses were calculated by using the XPS MultiQuant 7.0 program[42] utilizing the oxide-layer model. Inelastic mean free paths used in the calculations were obtained from the NIST Electron-Effective-Attenuation Length database.[43]

To determine the corrosion resistance of the weld beads, laser surface remelting treatments were performed with various compositions of shielding gas. The obtained 5083 remelted samples were subjected to polarization tests. Prior to these tests, the samples were grinded up to 120 grits to homogenize the testing surfaces and immersed in 3.5 pct NaCl at open circuit potential for 1 hour, with the purpose of reaching a stable corrosion potential. After this open circuit, the samples were polarized from –0.050 up to +0.400 V with respect to the open circuit potential at a polarization rate of 0.1667 mV $seconds^{-1}$. These measurements were performed with a potentiostat 1287 (Solartron ISA, Durham, U.K.) controlled by the software CorrWare 2.0 (Scribner Associates, Inc., Southern Pines, NC). The breakdown potential (E_p) and the polarization resistance (R_p) were estimated from the polarization curves.

Table I. Processing Parameters of High-Power Diode Laser

Laser Beam Configuration	Unit	Value
Emission mode	—	continuous wave
Laser light wavelength	nm	940 ± 10, 808 ± 10
Focus diameter	mm	2.04
Focal position	—	at specimen surface
Working distance	mm	69.3
Spot size on surface	mm^2	2.2 × 1.7
Weld bead length	mm	60

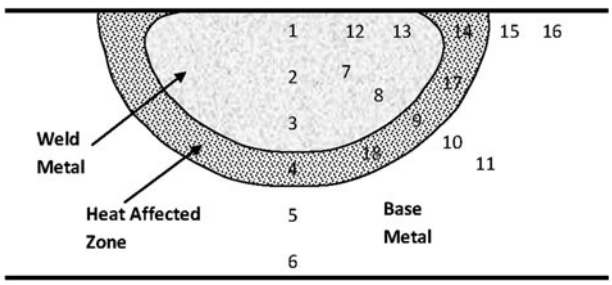

Fig. 2—Microhardness maps of 5083 weld beads.

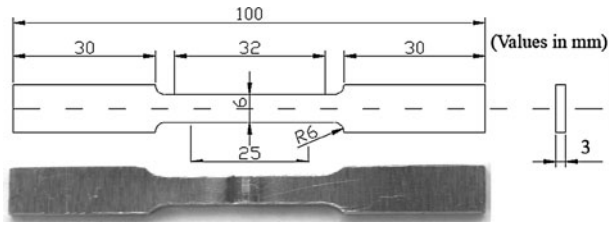

Fig. 3—Shape and size of the tensile strength test specimens prepared from welds.

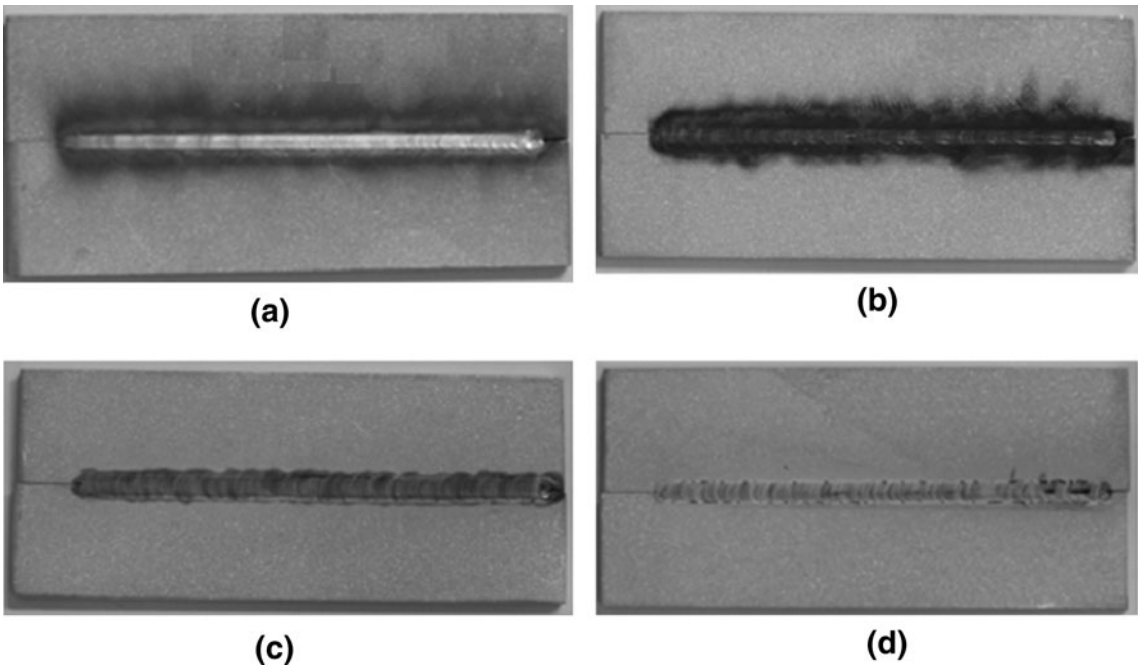

Fig. 4—Frontal view of 5083 samples processed with (*a*) 100 pct Ar, (*b*) 10 pct CO_2-90 pct Ar, (*c*) 40 pct CO_2-60 pct Ar, and (*d*) 100 pct CO_2.

III. RESULTS AND DISCUSSION

A. *Metallographic Study of the Butt Weld Beads*

To visualize the morphological aspect of the obtained welds in the presence of different CO_2 percentages, frontal views of the samples are presented in Figure 4. The pictures clearly illustrate the radical surface changes that occurred under different operating conditions. The use of pure argon as shielding gas generates a clean weld bead surface. No traces of oxides are visible to the naked eye as shown in Figure 4(a). At a low amount of CO_2, *i.e.,* 10 pct, the weld bead and its contour region are black (Figure 4(b)) and show a visible sign of carbon deposition (Eq. [1]). This is in agreement with several studies reporting that some metals such as barium, calcium, strontium, aluminum, copper, and magnesium can decompose a very small portion of CO_2 to carbon.[44] As the CO_2 amount in the shielding gas is above 40 pct, a continuous oxide layer (white color) is covering the bead surface and its periphery area as shown in Figures 4(c) and (d). When CO_2 is present at the shielding gas, an oxide layer can easily be formed on the weld surface because carbon dioxide reacts with the liquid-pool surface during the weld-pool solidification process. At a high temperature, oxygen may be produced from the decomposition of CO_2 (Eq. [2]), encouraging aluminum oxidation.[37] This reaction is highly endothermic and takes place only at high temperatures. The detection of aluminum oxides and magnesium oxides when carbon dioxide was used as shielding gas was afterward confirmed by means of XRD and XPS analyses (results shown later).

$$CO_2 \rightarrow C + O_2, \quad \Delta H^{\circ}_{298} = 394 \text{ kJ/mol} \qquad [1]$$

$$CO_2 \rightarrow CO + {}^{1}/_{2}O_2, \quad \Delta H^{\circ}_{298} = 552 \text{ kJ/mol} \qquad [2]$$

Additionally, the samples present cracks along the welding beads at a high concentration of CO_2 (above 30 pct). These cracks are thought to be caused by the tensions generated by the oxides formation during the solidification process.[16] This is in agreement with the works of Heiple and co-workers, who proposed that surface-active elements, such as oxygen, sulfur, selenium, and tellurium, can change the temperature coefficient of the surface tension for materials in the welding process.[45]

Figure 5 reports welding percentages in function of the amount of CO_2 in the shielding gas. The welding percentages parameter, measured macroscopically, depicts the ratio between the actual length of welded interface and the length of the interface exposed to the laser.[17] Thus, the welding percentage can range between 0 pct, when no joint is achieved, and 100 pct, when the specimens are totally welded. For instance, the linear laser scan is 60 mm long in our welding treatments. Thus, a value of welding percentage of 75 pct would mean that the weld generated is only 45 mm long (the remaining interface of 15 mm long not being successfully jointed). It could be checked in Figure 5 that when the percentage of CO_2 was higher than 40 pct, the samples were not totally welded (the welding percentage was below 100 pct).

Metallographic images of weld beads cross-sections, under different CO_2/Ar ratios in the shielding gas, are included in Figure 6. These metallographic images show that the progressive addition of CO_2 particularly increases the weld bead size of the samples. On the other hand, the shape of the butt welds is wide and

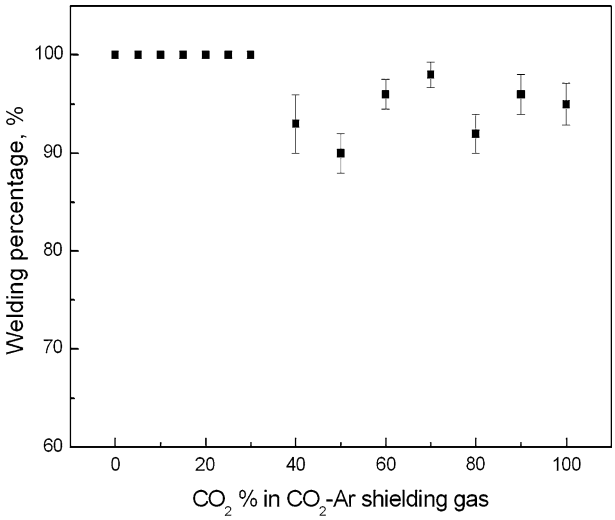

Fig. 5—Welding percentages of 5083 butt welds in function of CO_2 percentage.

shallow in all conditions and tends to be a semiellipse in which the ratio depth/width is lower than 0.5. This later morphological characteristic confirms that the weld beads are generated under a conduction regime.[14,21] It is also worthy to notice that the shielding gas composition has an observable influence on the solidified weld surface. Thus, the use of pure argon generates a plane surface, whereas the progressive increase of CO_2 in the shielding gas mixture remarkably modifies the form of the weld pool surface.

To observe the microstructural modifications, the AA5083 butt welds were analyzed with higher magnification by optical microscopy. Figure 7 includes optical micrographs of the sample welded with pure argon. The microstructural features of all welds were similar, regardless of the percentage of CO_2. The obtained microstructures are in good agreement with those previously reported for similar 5083 welds[16,17]; Figure 7(a) shows a general view of the three different zones: WM (Figure 7(d)), heat-affected zone (HAZ) (Figure 7(c)), and BM (Figure 7(b)). The different microstructures of these zones are provoked by the thermal processes of welding; the WM and HAZ undergo different heating/cooling rates and thus expansion/contraction.[16,17] Meanwhile, the external zones of the bead close to the BM (HAZ), Figure 7(c), are characterized by showing dendritic growth, which correspond to the zones with higher resolidification rates.[16] It can be also seen that the size of the precipitates decreases in the WM in comparison with the BM (Figure 7(d)). Additionally, an increase of the density of precipitates is observed in the WM. In other words, the laser welding process provokes a microstructural refinement in WM.[17] The microstructure of the different beads is seen to be similar, regardless of the percentage of CO_2 used. Therefore, the addition of CO_2 to the shielding gas mixture in the laser welding process does not seem to modify the microstructure refinement of the 5083 butt welds.

B. *SEM, TEM, and X-EDS Analysis*

In previous studies,[17] the authors have shown that laser treatments give rise to a microstructural refinement in 5083 aluminum alloy. In the current work, a higher magnification microstructural characterization of the obtained weld beads has been performed by SEM, TEM, and EDS. A similar microstructure has been observed in all weld beads, independently of the shielding gas composition. Figure 8 includes TEM images of BM, whereas Figure 9 shows TEM images of the WM (weld obtained with pure argon). It can be easily appreciated that the sizes of the precipitates of the WM (around 0.5 μm) are much smaller than those observed in the BM (around 2 μm). Thus, the intermetallic particles rich in Al, Mn, Fe, Si, and Cr of the 5083 BM appear in the inner part of the weld bead with a different shape and size. As a consequence of the fusion and solidification during laser welding, these intermetallic compounds are melted and resolidificated as smaller particles at the WM, and a fine microstructure is generated. By means of X-EDS semiquantitative analysis, the composition of these intermetallic compounds is also found to be different in both zones. The precipitates of the BM may have different compositions, some of them having a relatively high Fe and Mn content (6 to 10 pct Fe and 2 to 3 pct Mn). These precipitates, melted and resolidificated during the laser treatment, are of high interest because they are responsible for the corrosion phenomena called localized alkaline corrosion (LAC) in AA5083 samples.[46,47] Moreover, it is observed that the precipitates identified in the WM (Figure 9) contain less Fe and Mn (1 to 3 pct Fe and 0.5 to 1 pct Mn) than those observed in the BM. These observations are in good agreement with those recently reported by the authors.[17] To sum up, laser treatments provoke a microstructural refinement in 5083 samples so that the size, shape, and composition of the intermetallic compounds change. According to the microstructural characterization and to the SEM/X-EDS/TEM results, it seems that the nature of shielding gas does not influence the size/shape/composition of the intermetallic compounds appearing at the WM.

The magnesium content in BM and WM of the 5083 welds obtained with different CO_2/Ar shielding gases has been measured by X-EDS semiquantitative analysis as well. The percentages of magnesium loss in the WM with respect to BM are plotted in Figure 10 as a function of the CO_2 content in the shielding gas. The Mg content in WM is always lower than in BM, as a consequence of the Mg evaporation during the laser treatments. As can be observed in Figure 10, the magnesium losses ranges between 3.3 and 17 pct. The higher values of magnesium depletion were observed when the CO_2 content in the shielding gas was in the 40 to 60 pct range. With pure argon, the Mg loss is about 10.5 pct, whereas with pure CO_2 it is 7.9 pct. The lower magnesium evaporation (3.3 pct) corresponds to the sample shielded with 20 pct of CO_2. This condition seems to be the best, as Mg evaporation should always be minimized. In fact, Mg is reported to have a high

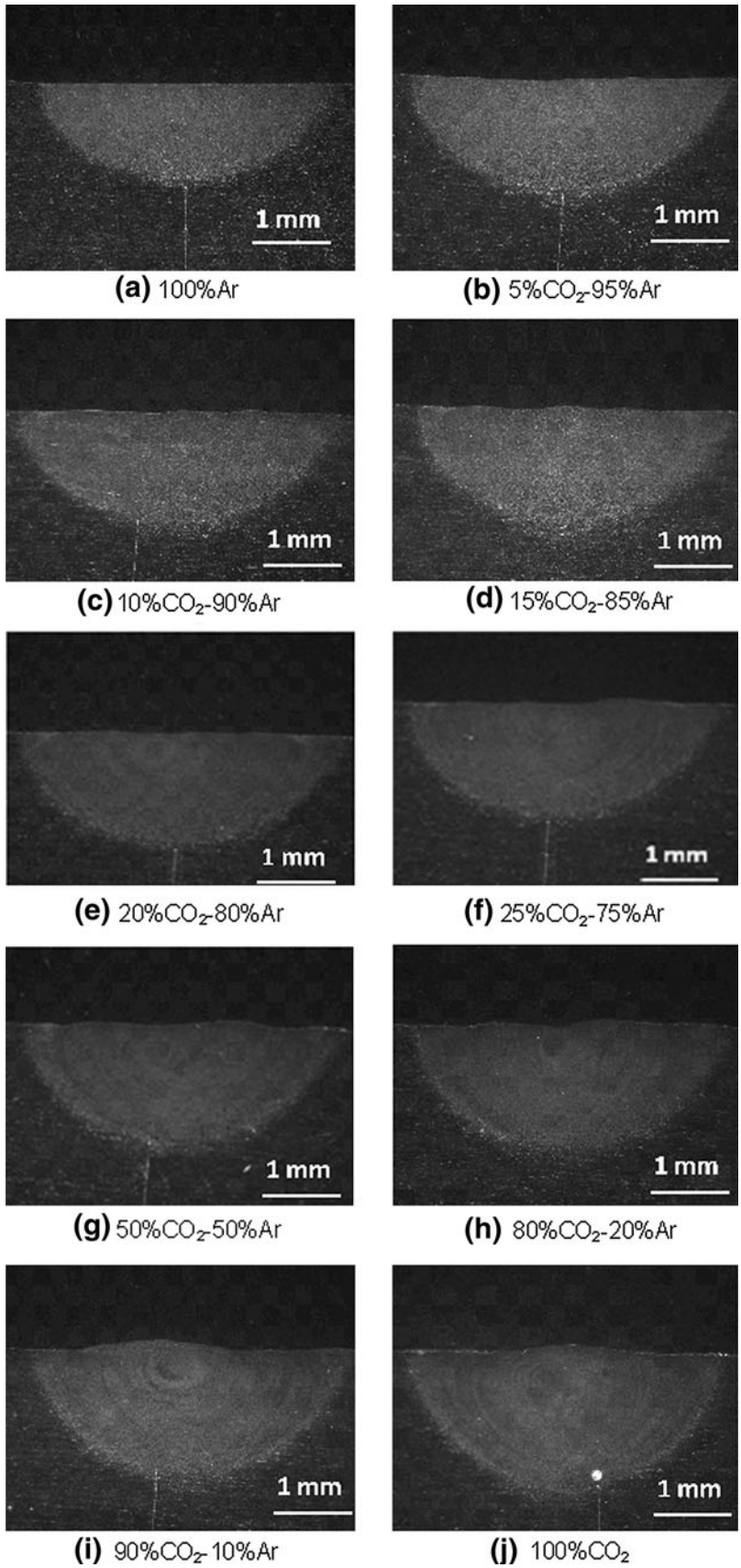

Fig. 6—Metallographic images of butt weld beads cross-sections for different CO_2 percentages in the shielding gas.

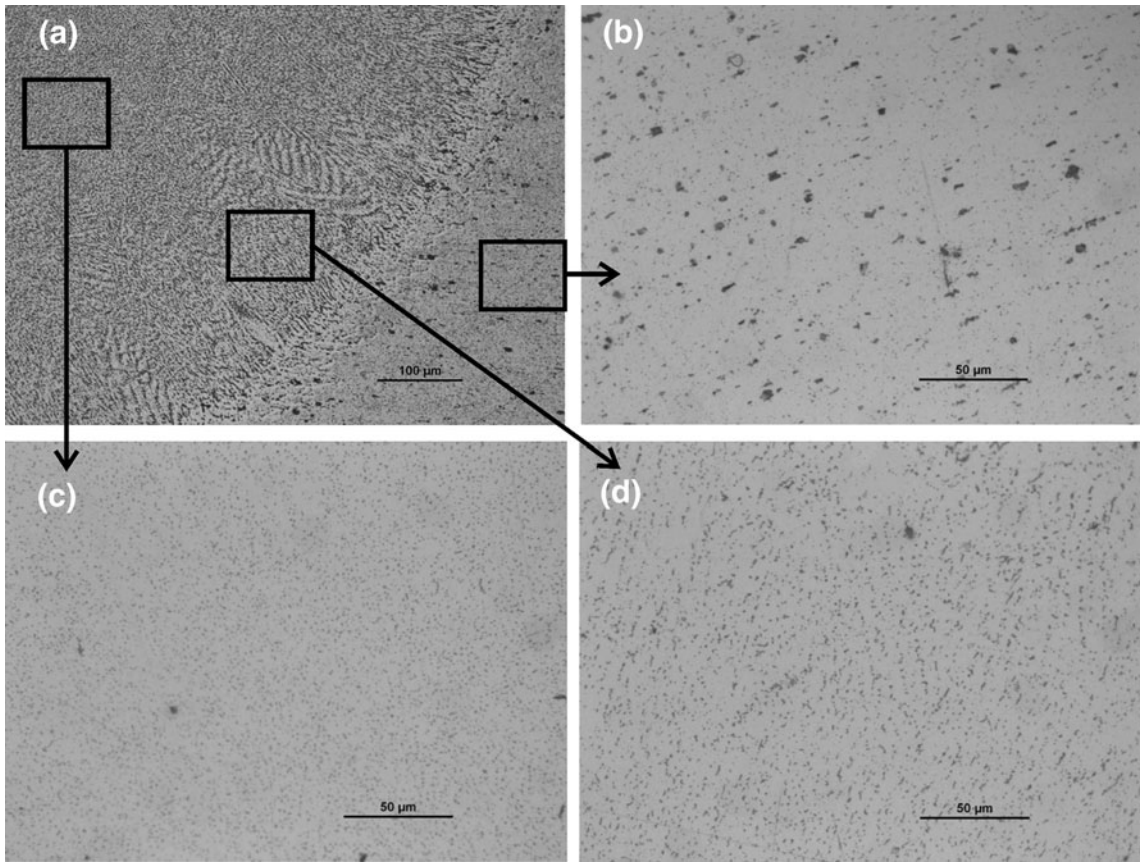

Fig. 7—Representative metallographic images of cross-section of 5083 butt weld, obtained at 1 m/min, P = 2 kW, using pure argon as shielding gas: (*a*) general view, (*b*) base metal, (*c*) heat-affected zone, and (*d*) weld metal.

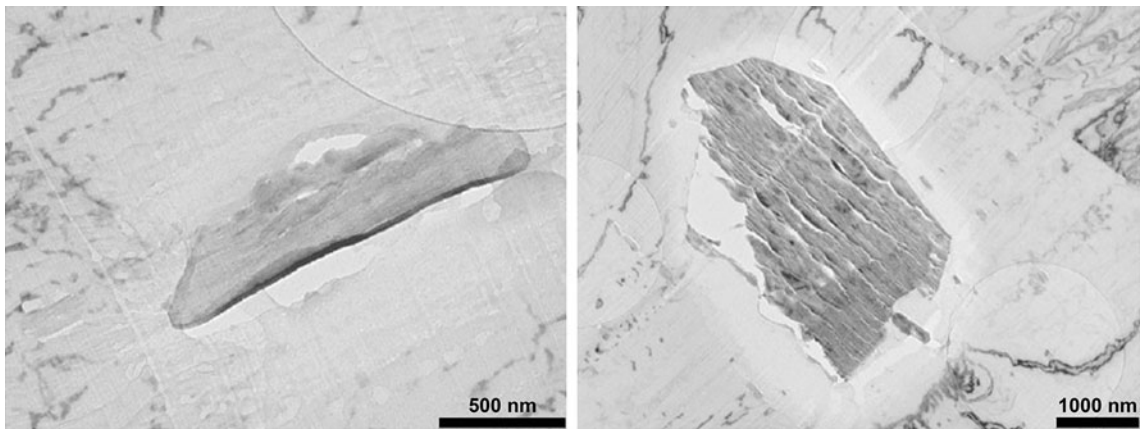

Fig. 8—TEM images of 5083 base metal.

importance for improving the weldability of aluminum alloys.[21]

C. *Macro-Structural (XRD) Characterization Studies*

The weld beads were also characterized by means of XRD. The spectra of the welds surfaces are reported in Figure 11. The X-ray diffraction patterns of 5083 alloy used as reference were found to be identical to the reference patterns reported in the literature (JCPDS 00.004.0787). The diffractogram is characterized by the presence of the typical peaks of aluminum as a unique crystalline phase (Figure 11(a)). On the contrary, new weak diffraction peaks are displayed in the 5083 weld bead shielded with argon, all of them assignable to $MgAl_2O_4$ (01.074.1132) and MgO (00.045.0946) phases

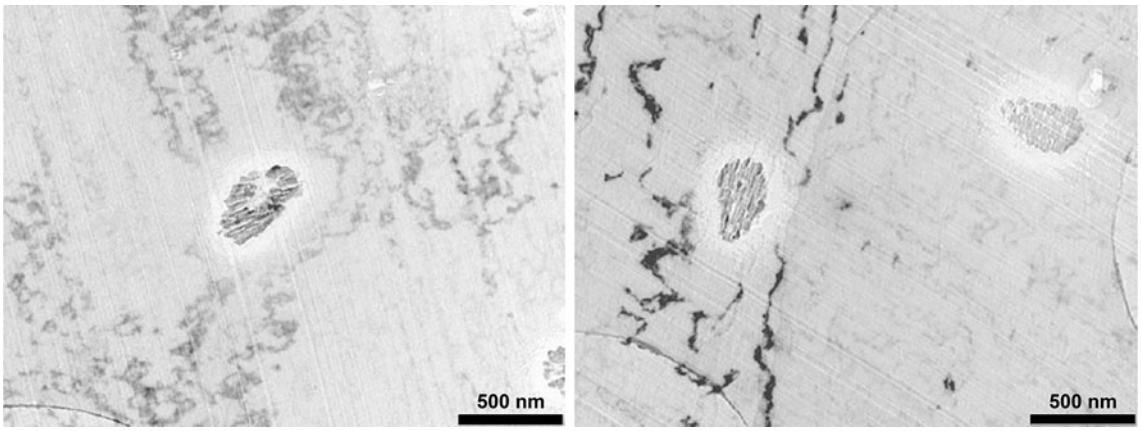

Fig. 9—TEM images of fused zone of 5083 welds obtained with pure argon.

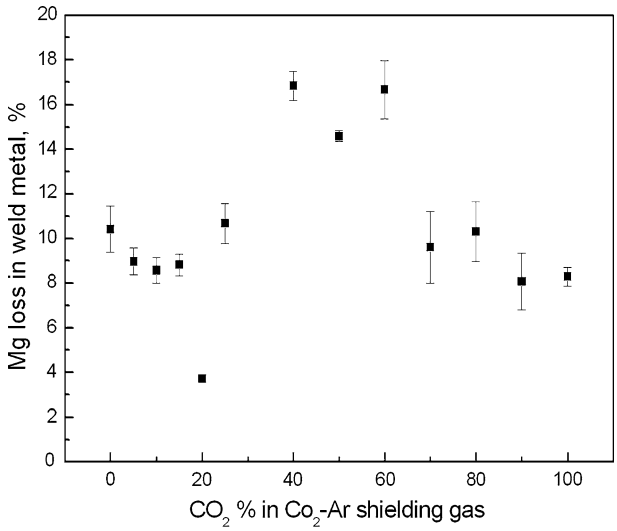

Fig. 10—Mg loss at different CO_2 pct in shielding gas.

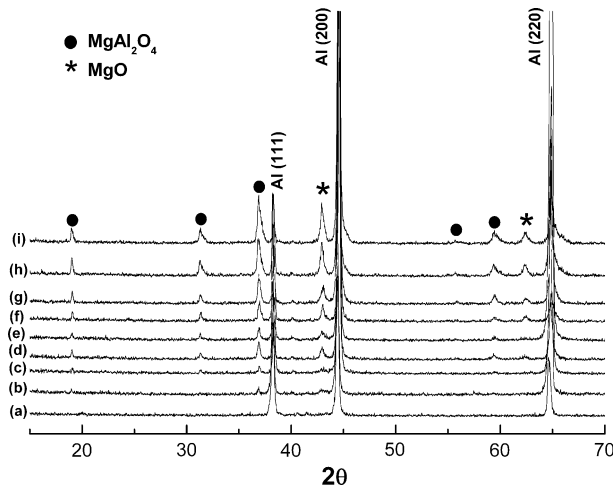

Fig. 11—X-ray diffractograms for (*a*) 5083 alloy used as reference and weld beads samples shielded by (*b*) Ar, (*c*) 5 pct CO_2, (*d*) 10 pct CO_2, (*e*) 20 pct CO_2, (*f*) 30 pct CO_2, (*g*) 50 pct CO_2, (*h*) 90 pct CO_2, and (*i*) 100 pct CO_2.

(Figure 11(b)). The use of CO_2-Ar mixtures as shielding gas shows remarkable differences with respect to those spectra reported in Figures 11(a) and (b). The intensities of the diffraction rays attributed to $MgAl_2O_4$ and MgO increase along with the concentration of CO_2 (Figures 11(b) through (i)). The effect of partial pressure of carbon dioxide may be explained by the dissociation of carbon dioxide and incorporation of chemisorbed oxygen into the alloy lattice presenting an oxygen source for MgO and $MgAl_2O_4$ formations.

The formation of these phases is also reported in earlier studies that claimed that magnesium aluminate spinel forms from its constituent oxides by diffusion of Al^{3+} and Mg^{2+} ions, starting around 1373 K (1100 °C) and is complete at around 1673 K (1400 °C).[48] On the other hand, the formation of MgO oxide suggests that the segregation is chemically driven by the greater affinity of Mg for O. Surprisingly, no peaks due to alumina crystalline phase are observed probably because the alumina generated is amorphous or because the sizes of diffracting domains are too small.

D. *XPS Studies*

The influence of the shielding gas on the weld beads surface composition has been investigated by means of XPS. Figure 12 reports wide scan survey XPS spectra of the AA5083 sample used as reference (Figure 12(a)) and the three weld beads samples shielded with 100 pct Ar (Figure 12(b)), 30 pct CO_2 - 70 pct Ar (Figure 12(c)), and 100 pct CO_2 (Figure 12(d)). Special attention has been paid to the distribution of aluminum oxidation state and the variation of Mg/Al molar ratio with the nature of shielding gas.

The Al 2p XPS spectra of these samples principally contain two peaks appearing around the BEs 74 eV and 72 eV, suggesting that Al is at least in two different oxidation states, Al (III) and Al (0), respectively (see Table II). Due to the different conductivity of the oxide layer and the substrate, the relative position of the peaks corresponding to the two different Al species changes. While charging effects can affect the position of the aluminum oxide Al 2p, the metallic aluminum substrate appears unaltered. BE data in Table II correspond to

corrected values for aluminum oxide component and uncorrected for the metallic component. The analysis of the aluminum element indicates that the addition of CO_2 to shielding gas composition increases the percentage of aluminum Al (III) *vs* Al (0). Therefore, the percentage of aluminum oxide detected by XPS increases from 87.3 pct when shielding with pure argon up to 100 pct when shielding with pure CO_2. The observed changes of the oxide-to-metal ratio could be related to changes in the oxide thickness as a function of the shielding gas composition. The thickness measurement of the oxide overlayer ranged from 7.1 nm when the weld bead was shielded with pure argon to more than 20 nm in the case of beads shielded with pure CO_2. These thicknesses were estimated by using the equation developed by Strohmeier,[49] assuming that more than 99.9 pct of aluminum oxide is calculated from the XPS signal.

Upon integration of the Mg 2s and Al 2p areas, the Mg/Al atomic ratios referred to similar sampling depths could be estimated. Table II summarizes these results, showing that the Mg/Al atomic ratios detected in the samples depend on the nature of the shielding gas. The increase of Mg/Al ratio was observed in all the welded samples in comparison with BM, suggesting that magnesium migrates to the surface region as result of thermal effect. Similarly, Saied and Sullivan showed that, in 1 pct Mg/Al alloy, the migration of Mg occurs toward the surface, resulting in a Mg-rich layer in the temperature range of 498 K to 623 K (225 °C to 350 °C).[50] Mg cations are in fact reported to have a much higher migration rate through the alumina layer than Al cations.[51,52] Note in Table II that the Mg/Al ratio value increases from 0.72 up to 4.20 when changing the shielding gas from pure argon to 30 pct CO_2. Hence, the use of CO_2 as shielding gas promotes the migration of Mg toward the surface and induces a surface magnesium enrichment of weld beads samples. This result is in good agreement with the observed increase of MgO and $MgAl_2O_4$ features in the XRD diffractograms reported in Figure 11.

E. *Depth and Width Measurements*

The detailed values of the width and depth of the butt welds shielded with different CO_2 contents are given in Figure 13. The dispersion (margin of error) of the measured values was always between 0.5 and 1 pct. It is generally appreciated that raising the CO_2 content in shielding gas leads to an increase in depth and width. In the case of pure CO_2, the depth reaches 1.65 mm and the width is 3.80 mm. The weld depth/width ratios (D/W) are also plotted *vs* the shielding gas content in Figure 14. This ratio is seen to increase as adding CO_2 to the shielding gas mixture. A ratio of 0.35 is obtained when

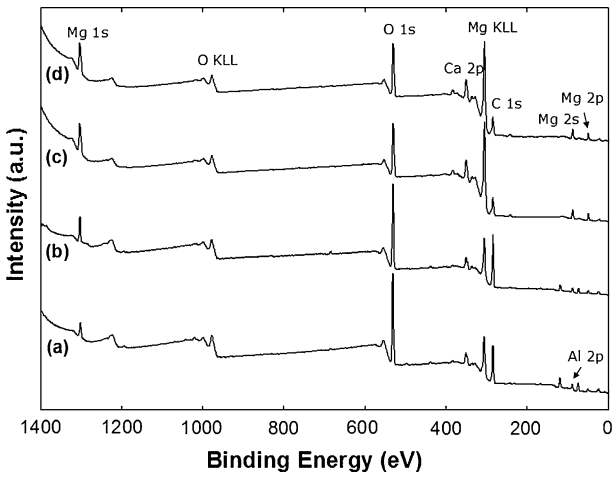

Fig. 12—XPS general spectra of (*a*) AA5083 and the weld beads samples shielded with (*b*) 100 pct Ar, (*c*) 30 pct CO_2-70 pct Ar, and (*d*) 100 pct CO_2.

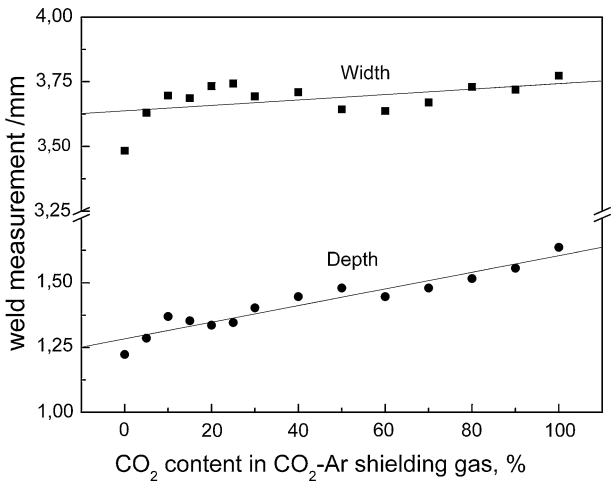

Fig. 13—Depth and width values of butt welding beads of 5083 samples *vs* the CO_2 additions.

Table II. Weld Beads XPS Analyses of AA5083 at Different Shielding Gas Compositions

	BE Al $2p_{3/2}$					
Sample	Al (III)	Al (0)	Pct Al (III)	Pct Al (0)	Mg 2s/Al 2p	Oxide Thickness (nm)
Reference	74.8	72.7	72.4	27.60	0.55	4.7
Ar	73.5	72.4	87.3	12.70	0.72	7.1
30 pct CO_2	73.3	71.2	88.0	12.00	4.20	7.5
100 pct CO_2	74.3	—	100	0.00	3.70	>20*

*Al(0) could not be detected, corresponding to thicknesses above 20 nm.[49]

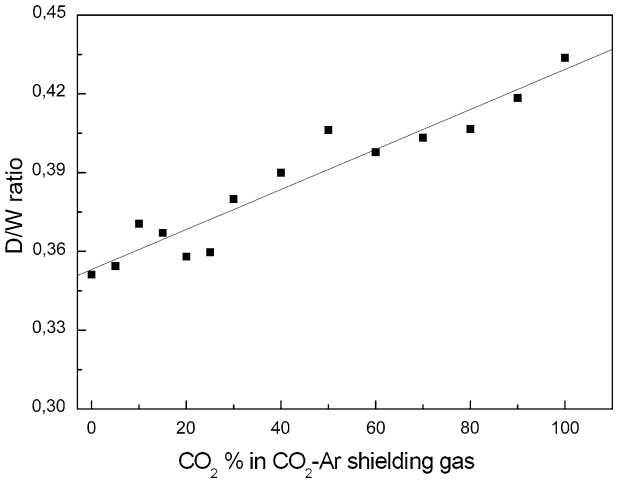

Fig. 14—Weld depth/width ratio under different CO_2 additions.

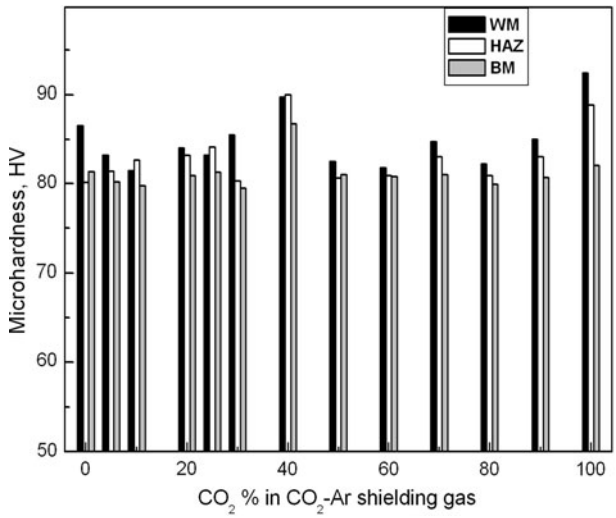

Fig. 15—Micro-hardness measurements of butt weld beads *vs* CO_2 content in CO_2-Ar shielding gas.

shielding with pure Ar and 0.43 when employing pure CO_2.

CO_2 and Ar have very different physical properties (heat conductivities, ionization potentials, *etc.*), and thus, the heat input provided to the workpieces may have changed when modifying the shielding gas composition. Therefore, it seems that the observed changes in weld bead size (Figure 13) can be related to the energy provided to fuse the metal; the energy values increase as the amount of CO_2 is enhanced. In addition to this argument and taking into account that welds are generated under a conduction regime, the authors think that the limited Marangoni convection due to the oxide formation (oxide formation being encouraged as increasing CO_2) can also influence the final morphology of the weld.

The literature reported that the Marangoni forces in the liquid weld pool modulate the final bead penetration.[45,53–55] Shanping *et al.* studied the effects of CO_2 additions on GTA weld shape of stainless steel and ascribed them to three different models managing the liquid pool convection: (1) quasi-free pool surface with an outward Marangoni convection (when the CO_2 is in the range of 0 to 0.2 pct), (2) quasi-free pool surface with an inward Marangoni convection ($0.2 < CO_2 < 0.6$ pct), and (3) restricted pool surface with heavy continuous oxide layer ($CO_2 > 0.6$ pct).[55] In other work, Shanping *et al.* showed that the weld D/W ratio should decrease due to the inward Marangoni convection pattern and increase due to the outward Marangoni convection pattern.[56]

It is widely known that weld pool of aluminum alloys normally has an outward Marangoni convection pattern. Our investigation shows that the progressive addition of CO_2 to Ar produces a continuous oxide layer on the weld pool surface. In agreement with a previous study, the oxide formed becomes a barrier for the shielding gas conveyance to the weld pool.[55] In these conditions, the liquid pool/oxide layer interface is present instead of the liquid pool/gas surface; the Marangoni convection in the periphery area becomes limited. We can conclude that in the range of CO_2 concentrations used in this work (5 to 100 pct), the convection forces slightly change with CO_2 additions to shielding gas mixture. Thus, although the convection model does not change, when increasing CO_2 in the shielding gas, the outward Marangoni convection at the weld surface is more limited, leading to progressive increase of D/W ratio (Figure 14). Furthermore, the observed higher weld penetration values as increasing CO_2 in the shielding gas (Figure 13) is explained taking into account the higher input energy provided by the CO_2 to the weld zone.

F. *Mechanical Properties of the Butt Welds*

Microhardness tests were performed on cross-sections, according to the scheme of Figure 2, to characterize the WM, HAZ, and BM. The Vickers microhardness values obtained for each zone have been averaged and included in Figure 15 for the different percentages of CO_2 used as a shielding gas. As can be observed, the microhardness values of the weld bead are slightly higher than the values of the BM surrounding the bead in all cases. These results agree with those reported in References 16 and 17. The little differences between the microhardness of the fusion zone (composed of WM and HAZ) and the surrounding BM are related to the microstructural changes described above. Hence, the microstructural refinement of the fusion zone leads to a microhardness increase of around 5 HV under all shielding gas conditions, except when employing pure CO_2, in which an increase of 12 HV is measured.

Figure 16 depicts the ultimate tensile strength (UTS) of the welds shielded with different CO_2/Ar ratios. The tensile strength of the 5083 alloy has been determined to be 280 MPa (average UTS value of not-welded sample). This reference is in good agreement with the results reported in the literature.[57] Generally, the progressive addition of CO_2 in the CO_2-Ar shielding gas mixture

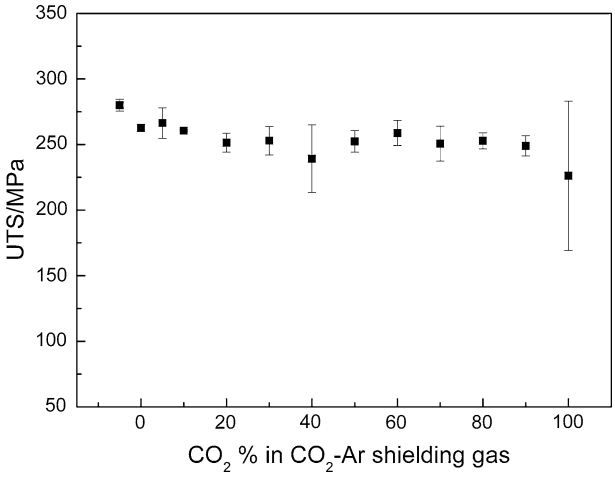

Fig. 16—UTS of 5083 welded samples shielded with different CO_2 pct in the CO_2-Ar shielding gas mixture.

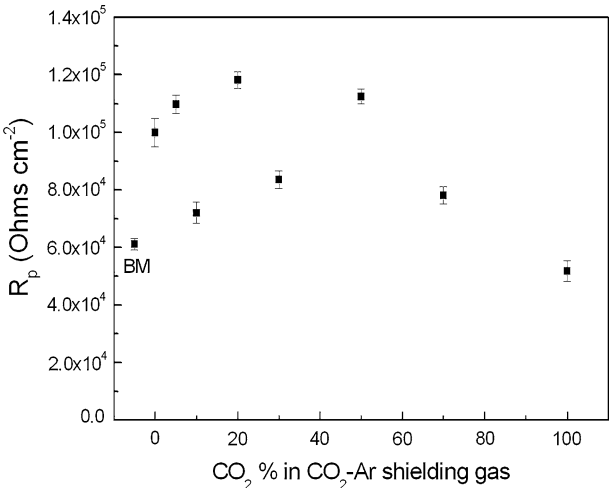

Fig. 17—R_p values of samples laser remelted with different CO_2-Ar shielding gas composition.

does not modify the strength properties of 5083 welds in comparison with the use of pure argon. However, the use of pure CO_2 produces a weld bead with relatively low tensile strength in comparison with argon. This result may be explained by the relatively high hardness contrast between the BM and WZ in the case of the weld shielded with CO_2.

In general terms, reasonably good welds are obtained under the welding conditions employed here, as joint samples show similar UTS to the reference BM. In fact, except for pure CO_2, all the conditions leaded to welds with UTS values around 90 pct of the UTS value of the reference BM.

G. *Corrosion Resistance*

R_p is a parameter inversely proportional to the corrosion rate strictly in the case of systems that corrode uniformly under activation control. However, even in localized corrosion processes, it is usually inversely proportional to the corrosion activity; the systems with lower electrochemical activity have higher R_p values. The R_p values of remelted 5083 samples shielded with different CO_2-Ar mixtures have been plotted in Figure 17. Regardless of the shielding gas composition, it seems that all remelted samples present higher R_p values and therefore better corrosion behavior than untreated 5083 BM. Only the samples shielded with pure CO_2 show similar R_p to the reference. The R_p increase observed in most samples is due to microstructural refinement, which causes a change in the size, composition and distribution of intermetallic compounds. According to References 46 and 47, some intermetallic compounds of this alloy present a cathodic behavior with respect to the BM, leading to localized alkaline corrosion processes. The intermetallic compounds are melted and resolidificated within the laser treatment, providing surfaces with improved corrosion behavior.[17]

The results prove that considerable improvement of the corrosion resistance could be achieved by laser surface remelting, especially when shielding with 20 pct CO_2-80 pct Ar. This condition is the one providing higher R_p values. It can be explained recalling the Mg loss measurements reported above. Thus, these samples are the ones presenting lower magnesium loss. This result match with our previous studies,[16] in which the aluminum welds (generated also under conduction regime) with the highest magnesium content showed the best corrosion-resistance behavior.

Moreover, we have determined the values of the breakdown potential (E_p) at current density of 10^{-4} A/cm^2. This parameter is related to another type of localized corrosion known as crystallographic pitting.[46,47] E_p values are seen to be similar in all samples (treated and untreated) (–0.69 V), reflecting that this corrosion mechanism is kept in all samples. In fact, the literature[47] indicates that the crystallographic pitting corrosion is not affected by the cathodic precipitates. Therefore, E_p seems to depend only on the aluminum matrix properties, being unaffected by the various treatments carried out.

IV. CONCLUSIONS

The influence of shielding gas composition on the weld quality of 5083 samples has been investigated. The AA 5083 weld bead samples, shielded by different CO_2-Ar gas mixtures, have been characterized by metallographic/microstructural studies, XRD, X-EDS chemical analyses, XPS, microhardness measures, tensile strength, and corrosion-resistance tests. The analysis of the obtained results has allowed us to conclude that butt weld properties of AA5083 samples can be modulated by modifying the shielding gas composition.

The additions of CO_2 to the shielding gas mixture in the laser welding process do not modify the microstructure refinement of the 5083 butt welded alloy and do not affect significantly its mechanical properties (strength and microhardness), whereas it increases the weld penetration, and produces the oxidation of the liquid

pool surface. XRD analyses confirmed the formation of predominant oxides phases, $MgAl_2O_4$ and MgO, in weld beads surface when the laser welding was processed employing CO_2 in shielding gas mixtures.

XPS was successfully used to investigate the surface of weld bead samples. It was found that the surface composition was affected significantly by CO_2 additions. The distribution of aluminum between its two different forms (metallic and oxidized) depends on the nature of the shielding gas. The addition of CO_2 to the shielding gas also promotes the migration of Mg toward the surface and increases the oxide layer thickness.

Furthermore, the current study clearly demonstrates that laser surface remelting in presence of CO_2-Ar gas mixtures could be a suitable tool to improve corrosion resistance of AA5083. The results proved that improvement of the corrosion resistance could be achieved by laser surface remelting, as a consequence of the microstructural refinement. The best corrosion resistance was reached in the presence of 20 pct CO_2-80 pct Ar as shielding gas, due to the lowest magnesium reduction.

The overall results reported in this article indicate that the employment of CO_2-Ar mixtures as shielding gas is a potential way to improve the efficiency of laser welding of aluminum alloys. The best combination of mechanical and corrosion properties of welds have been obtained when shielding with 20 pct CO_2-80 pct Ar.

ACKNOWLEDGMENTS

The current work has been financially supported by the Ministerio de Educación y Ciencia (project DELATIAL, Ref. MAT2008-06882-C04-02) and by the Junta de Andalucía (project SOLDATIA, Ref. TEP 6180).

REFERENCES

1. J.M. Sánchez-Amaya, M.R. Amaya-Vázquez, and F.J. Botana: *Handbook of Laser Welding Technologies*, 1st ed., Woodhead Publishing, Cambridge, U.K., 2013, pp. 215–18.
2. F. Matsuda and K. Nakata: *Trans. JWRI*, 1995, vol. 24 (1), pp. 83–94.
3. W. van Haver, X. Stassart, J. Verwimp, B. De Meester, and A. Dhooge: *Weld. World*, 2006, vol. 50 (11–12), pp. 65–77.
4. U. Dilthey, A. Brandenburg, and F. Reich: *Weld. World*, 2006, vol. 50 (7–8), pp. 7–10.
5. F.S. Bayraktar and P.S. Staron: *Weld. World*, 2007, vol. 51 (1–2), pp. 28–34.
6. H. Zhao and T. DebRoy: *Metall. Mater. Trans. B*, 2001, vol. 32B, pp. 163–72.
7. Y. Shi, F. Zhonga, X. Li, S. Gong, and L. Chen: *Mater. Sci. Eng. A*, 2007, vol. 465, pp. 153–59.
8. P. Bassani, E. Capello, D. Colombo, B. Previtali, and M. Vedani: *Compos. Part A*, 2007, vol. 38, pp. 1089–98.
9. R. Spina, L. Tricarico, G. Basile, and T. Sibillano: *J. Mater. Proc. Tech.*, 2007, vol. 191, pp. 215–19.
10. A. Ancona, T. Sibillano, L. Tricarico, R. Spina, P.M. Lugara, G. Basile, and S. Schiavone: *J. Mater. Proc. Tech.*, 2005, vols. 164–165, pp. 971–77.
11. T. Sibillano, A. Ancona, V. Berardia, E. Schingaro, G. Basilea, and P.M. Lugara: *Opt. Lasers Eng.*, 2006, vol. 44, pp. 1039–51.
12. L. Tricarico, R. Spina, D. Sorgente, A. Ancona, T. Sibillano, and G. Basile: *Key Eng. Mater.*, 2007, vol. 344, pp. 745–50.
13. A. Haboudou, P. Peyre, A.B. Vannes, and G. Peix: *Mater. Sci. Eng. A*, 2003, vol. 363, pp. 40–52.
14. E. AssunÇao, S. Williams, and D. Yapp: *Opt. Lasers Eng.*, 2012, vol. 50, pp. 823–28.
15. R. Akhter, L. Ivanchev, and H.P. Burger: *Mater. Sci. Eng. A*, 2007, vol. 447, pp. 192–96.
16. J.M. Sánchez-Amaya, T. Delgado, J.J. De Damborenea, V. López, and F.J. Botana: *Sci. Technol. Weld. Joi.*, 2009, vol. 14 (1), pp. 78–86.
17. J.M. Sánchez-Amaya, T. Delgado, L. González-Rovira, and F.J. Botana: *Appl. Surf. Sci.*, 2009, vol. 255 (23), pp. 9512–21.
18. N. Abe, M. Tsukamoto, K. Maeda, K. Namba, and J. Morimoto: *J. Laser Appl.*, 2006, vol. 18 (4), pp. 289–93.
19. K. Howard, S. Lawson, and Y. Zhou: *Weld. J.*, 2006, vol. 85 (5), pp. 101–10.
20. J.M. Sánchez-Amaya, Z. Boukha, L. González-Rovira, J. Navas, J. Martín-Calleja, and F.J. Botana: *J. Laser Appl.*, 2012, vol. 24 (1), pp. 012002–09.
21. J.M. Sánchez-Amaya, Z. Boukha, M.R. Amaya-Vázquez, and F.J. Botana: *Weld. J.*, 2012, vol. 91 (5), pp. 155–61.
22. T. Nacey: *Weld. J.*, 2001, vol. 6, pp. 28–30.
23. L. Li: *Opt. Laser. Eng.*, 2000, vol. 34, pp. 231–53.
24. H. Wang, Y. Shi, S. Gong, and A. Duan: *J. Mater. Process. Tech.*, 2007, vol. 184, pp. 379–85.
25. E. Akman, A. Demir, T. Canel, and T. Sınmazcelik: *J. Mater. Process. Tech.*, 2009, vol. 209, pp. 3705–13.
26. L. Shanping, F. Hidetoshi, and N. Kiyoshi: *ISIJ Int.*, 2005, vol. 45 (1), pp. 66–70.
27. B.E. Paton: *Avtom. Svarka.*, 1974, vol. 6, pp. 1–7.
28. W.S. Bennett and G.S. Mills: *Weld. J.*, 1974, vol. 53, pp. 548–53.
29. B.G. Chung, S. Rhee, and C.H. Lee: *Mater. Sci. Eng. A-Struct.*, 1999, vol. 272 (2), pp. 357–62.
30. S. Katayama, H. Nagayama, M. Mizutani, and Y. Kawahito: *Weld. Int.*, 2009, vol. 23 (10), pp. 744–52.
31. A. Matsunawa, S. Katayama, and K. Kojima: *Weld. Res. Abroad*, 1999, vol. 45 (8), pp. 2–11.
32. G. Tani, A. Ascari, G. Campana, and A. Fortunato: *Appl. Surf. Sci.*, 2007, vol. 254 (4), pp. 904–07.
33. W.F. Savage, E.F. Nippes, and G.M. Goodwin: *Weld. J.*, 1977, vol. 56, pp. 126–32.
34. C.R. Heiple and J.R. Roper: *Weld. J.*, 1981, vol. 60, pp. 143–45.
35. Y. Takeuchi, R. Takagi, and T. Shinoda: *Weld. J.*, 1992, vol. 71, pp. 283–89.
36. D.H. Abbott and C.E. Albright: *J. Laser. Appl.*, 1994, vol. 6 (2), pp. 69–80.
37. L. Shanping, F. Hidetoshi, and N. Kiyoshi: *Metall. Mater. Trans. A*, 2004, vol. 35A, pp. 2861–67.
38. M.J. Tobar, I.M. Lamas, A. Yáñez, J.M. Sánchez-Amaya, Z. Boukha, and F.J. Botana: *Phys. Procedia*, 2010, vol. 5 (2), pp. 299–308.
39. J.M. Sánchez-Amaya, Z. Boukha, M.R. Amaya-Vázquez, L. González-Rovira, and F.J. Botana: *Mater. Sci. Forum*, 2012, vol. 713, pp. 7–12.
40. J.M. Sánchez-Amaya, Z. Boukha, L. González-Rovira, M.R. Amaya-Vázquez, and F.J. Botana: *Adv. Mater. Res.*, 2012, vol. 498, pp. 37–42.
41. ASTM E-384, "Standard Test Method for Micro-indentation Hardness of Materials", 1999.
42. M. Mohai: *Surf. Interface Anal.*, 2004, vol. 36, pp. 828–32.
43. C.J. Powell and A. Jablonski: *NIST Electron-Effective-Attenuation Length Database*, Version 1.3, SRD 82, National Institute of Standards and Technology, Gaithersburg, MD, 2011, pp. 24–25.
44. M. Tsuji, T. Yamamoto, Y. Tamaura, T. Kodama, and Y. Kitayama: *Appl. Catal. A: Gen.*, 1996, vol. 142, pp. 31–45.
45. C.R. Heiple and J.R. Roper: *Weld. J.*, 1982, vol. 61, pp. 97–102.
46. A. Aballe, M. Bethencourt, F.J. Botana, M. Marcos, and J.M. Sánchez-Amaya: *Corros. Sci.*, 2004, vol. 46, pp. 1909–20.
47. A. Aballe, M. Bethencourt, F.J. Botana, M.J. Cano, and M. Marcos: *Corros. Sci.*, 2001, vol. 43, pp. 1657–74.
48. R. Naghizadeha, H.R. Rezaie, and F. Golestani-Fard: *Ceram. Int.*, 2011, vol. 37 (1), pp. 349–54.
49. B.R. Strohmeier: *Surf. Interf. Anal.*, 1990, vol. 15, pp. 51–56.

50. S.O. Saied and J.L. Sullivan: *J. Phys. Condens. Mater.*, 1993, vol. 5, pp. 165–66.
51. J.M. Sánchez-Amaya, G. Blanco, F.J. Garcia-Garcia, M. Bethencourt, and F.J. Botana: *Surf. Coat. Tech.*, 2012, vol. 213, pp. 105–16.
52. F.J. Garcia-Garcia, E.V. Koroleva, G.E. Thompson, and G.C. Smith: *Surf. Interface Anal.*, 2010, vol. 42, pp. 258–63.
53. P. Sahoo, T. DebRoy, and M.J. McNallan: *Metall. Trans. B.*, 1988, vol. 19B, pp. 483–91.
54. K. Ishizaki, N. Araki, and H. Murai: *J. Jpn. Weld. Soc.*, 1965, vol. 34, pp. 146–53.
55. L. Shanping, F. Hidetoshi, and N. Kiyoshi: *J. Mater. Sci.*, 2005, vol. 40, pp. 2481–85.
56. L. Shanping, F. Hidetoshi, T. Manabu, and N. Kiyoshi: *Trans. JWRI.*, 2004, vol. 33 (1), pp. 5–9.
57. S. Hassanifard and M. Zehsaz: *Procedia Eng.*, 2010, vol. 2, pp. 1077–85.